

Machine-learned model Hamiltonian and strength of spin–orbit interaction in strained Mg_2X ($\text{X} = \text{Si}, \text{Ge}, \text{Sn}, \text{Pb}$)

Mohammad Alidoust^{1,*} , Erling Rothmund¹ and Jaakko Akola^{1,2}

¹ Department of Physics, Norwegian University of Science and Technology, N-7491 Trondheim, Norway

² Computational Physics Laboratory, Faculty of Natural Sciences, Tampere University, FI-33101 Tampere, Finland

E-mail: phymalidoust@gmail.com

Received 8 April 2022, revised 25 May 2022

Accepted for publication 17 June 2022

Published 1 July 2022



Abstract

Machine-learned multi-orbital tight-binding (MMTB) Hamiltonian models have been developed to describe the electronic characteristics of intermetallic compounds Mg_2Si , Mg_2Ge , Mg_2Sn , and Mg_2Pb subject to strain. The MMTB models incorporate spin–orbital mediated interactions and they are calibrated to the electronic band structures calculated via density functional theory by a massively parallelized multi-dimensional Monte-Carlo search algorithm. The results show that a machine-learned five-band tight-binding (TB) model reproduces the key aspects of the valence band structures in the entire Brillouin zone. The five-band model reveals that compressive strain localizes the contribution of the $3s$ orbital of Mg to the conduction bands and the outer shell p orbitals of X ($\text{X} = \text{Si}, \text{Ge}, \text{Sn}, \text{Pb}$) to the valence bands. In contrast, tensile strain has a reversed effect as it weakens the contribution of the $3s$ orbital of Mg and the outer shell p orbitals of X to the conduction bands and valence bands, respectively. The π bonding in the Mg_2X compounds is negligible compared to the σ bonding components, which follow the hierarchy $|\sigma_{sp}| > |\sigma_{pp}| > |\sigma_{ss}|$, and the largest variation against strain belongs to σ_{pp} . The five-band model allows for estimating the strength of spin–orbit coupling (SOC) in Mg_2X and obtaining its dependence on the atomic number of X and strain. Further, the band structure calculations demonstrate a significant band gap tuning and band splitting due to strain. A compressive strain of -10% can open a band gap at the Γ point in metallic Mg_2Pb , whereas a tensile strain of $+10\%$ closes the semiconducting band gap of Mg_2Si . A tensile strain of $+5\%$ removes the three-fold degeneracy of valence bands at the Γ point in semiconducting Mg_2Ge . The presented MMTB models can be extended for various materials and simulations (band structure, transport, classical molecular dynamics), and the obtained results can help in designing devices made of Mg_2X .

Keywords: intermetallic materials, first-principle calculations, low-energy models

(Some figures may appear in colour only in the online journal)

1. Introduction

Intermetallic compounds Mg_2X ($\text{X} = \text{Si}, \text{Ge}, \text{Sn}$) are mainly considered to be semiconductors and their addition to, e.g.

metallic matrices can form solid solutes and grains. These Mg_2X solid solutes can desirably change the electronic, mechanical, and macroscopic properties of these metallic matrices [1–6]. Furthermore, Mg_2X ($\text{X} = \text{Si}, \text{Ge}, \text{Sn}$) are chemically and thermally stable, nontoxic, resistive against oxidation, economically inexpensive, environmentally friendly,

* Author to whom any correspondence should be addressed.

relatively light weight, and therefore have a great potential for large-scale production [2, 7, 8]. More importantly, they possess a high figure of merit (thermoelectric performance in a device form) and can serve as good solid-state thermoelectric materials for converting waste heat to electricity. These excellent characteristics have fuelled robust effort to explore various aspects of Mg_2X and find ways to improve and optimize their favorable performance. For instance, one main approach followed to manipulate the electrical transport of these compounds was by intercalation with differing elements [4, 5, 7–20]. It was found that the intercalation can result in nonlinearity in the band gap, enhanced spin–orbit interaction (SOI), and band splitting. The controllable and efficient thermoelectric materials are promising in designing micro-scale self-powered sensors, solar thermal elements, and waste heat recovery devices [21–29].

There has been an intensive theoretical effort to study these compounds, mainly using density functional theory (DFT) [1, 14, 15, 30–38]. The theoretical studies can provide deep and independent insight into the physics of these compositions and shed light on delicate aspects. For example, one can attain a better view over the physical mechanisms and possibly harnessing them in the future experiments, to create new opportunities, achieve more reliable analysis, and avoid introducing detrimental effects during the implementation process. Additionally, there are multiple works discussing various aspects of these compounds by using an effective single-band parabolic approximation [6, 8, 14]. The common assumption of these works is the homogeneity of the alloys and generalization of the rigid-band structure approach to obtain the band structure of the intermediate alloy systems.

Motivated by the above, we have constructed machine-learned multi-orbital tight-binding (MMTB) models, accounting for the $\{s, p, d, s^*\}$ orbitals and SOI. The parameters of the models are determined through optimizing it to DFT band structures by a massively parallelized multi-dimensional Monte-Carlo search algorithm. Our investigations demonstrate that a simple machine-learned five-band tight-binding (TB) model is sufficient to describe the electronic properties of strained Mg_2X ($\text{X} = \text{Si}, \text{Ge}, \text{Sn}, \text{Pb}$) close to the Fermi level. The results of the model show that compressive (tensile) strain enhances (suppresses) the SOI strength in Mg_2X . The Mg – X interactions were found to dominate over Mg – Mg and X – X counterparts. The π bonding is negligible whereas the dominant variation against strain appears in σ_{pp} . We have found that a tensile strain on the order of $\varepsilon = 5\%$ eliminates the three-fold degeneracy of the valence bands at the Γ point in Mg_2Ge . A two-fold band degeneracy, however, remains intact throughout $\varepsilon \in [-10\%, +10\%]$ in Mg_2Si . Our results illustrate that the band gap of Mg_2X is highly tunable through a uniform strain so that, despite their unstrained characteristics, the Mg_2X compounds can acquire semiconductor (metallic) characteristics. These findings point into an excellent opportunity for band engineering of Mg_2X -based materials [29] and can be helpful when analyzing and designing devices made of Mg_2X .

Moreover, unlike the simple single-band parabolic models, our machine-learned five-band TB model is able to capture

key features of the DFT valence band structure of strained Mg_2X ($\text{X} = \text{Si}, \text{Ge}, \text{Sn}, \text{Pb}$) within the entire Brillouin zone with significantly reduced computational complications and lower cost than DFT. Therefore, it can be employed to perform large-scale molecular dynamics simulations and quantum transport studies as further improvements are desired for a practical implementation of Mg_2X -based thermoelectric generators, which are of fundamental importance from the engineering and technical points of view. Methodologically, our approach is transferable for Mg_2X -related intercalation compounds and it provides a basis for developing more realistic TB models than the single-band parabolic models. We remark that the DFT method itself is applicable for systems with few hundreds of atoms and once different elements are included, the calculations for searching favorable compositions become computationally very challenging if not impossible [39]. From the technical and fundamental physics perspectives, the MMTB approach discussed in this paper has a very low computational cost, it provides an explicit Hamiltonian that can accommodate an external magnetic field, many-body interactions, impurities and disorder, and thereby, it facilitates real space simulations, which are relevant for experiments. Furthermore, this approach provides highly deep and fundamental physical insights into the electronics properties and interactions that can occur in a system such as the detailed orbital interactions briefly discussed and shall be presented at length in the following.

The paper is organized as follows. In section 2, we discuss the configuration, crystal symmetry of Mg_2X , and the displacement vectors used in our MMTB models. In section 3, the TB formalism is summarized. In sections 4 and 5, the Monte-Carlo search algorithm and details of the DFT calculations are given, respectively. The results are presented in section 6 and finally, the concluding remarks are summarized in section 7.

2. Configuration of Mg_2X

Figure 1 displays the configuration of Mg_2X with two different views. Figure 1(a) shows the top view of the structure whereas figure 1(b) is a three-dimensional perspective view. The structure is equivalent to the fluorite structure with the anions and cations swapped and is known as antiferite. An antiferite configuration can be generated with a face-centered cubic Bravais lattice and a simple-cubic lattice in the interstitial sites. The X atoms are located on the atom sites of the former lattice while the Mg atoms occupy the atom sites of the latter lattice. In what follows, for simplifying our notation, we have labeled the cation sublattice sites by A (A') (two atoms per unit cell) and the anion sublattice site by B (one atom per unit cell). As seen in figure 1, the unit cell of Mg_2X contains twelve atoms (8:4 ratio). To construct an accurate TB model, one needs to account for both the different atom types available in a composition and the distance and orientation of different atoms with respect to other atoms. Defining the TB interaction vectors, we have summarized the nearest-neighbor interaction vectors $\delta_{\alpha\beta}$ among atoms located

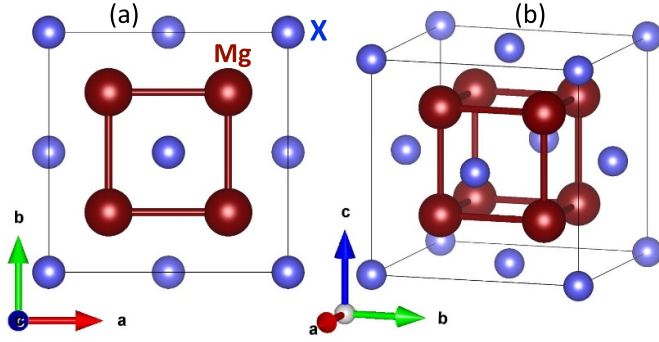


Figure 1. The configuration of the M_2X compounds. The magenta and blue spheres display the Mg and X atoms, respectively. Panel (a) shows the top view of the structure and panel (b) is a three-dimensional view of the same structure. The principal axes are marked by a, b, c. The lattice constant is a , which connects two X atoms along each principal axis.

Table 1. Nearest-neighbor vectors $\delta_{\alpha\beta}$ among the sites of the sublattices A, A', B. The lattice constant is denoted by a .

α	β	(x, y, z)	α	β	(x, y, z)
A	A'	$a(\pm 1, 0, 0)/2$	B	B	$\pm a(0, 1, 1)/2$
A'	A	$a(0, \pm 1, 0)/2$			$\pm a(1, 0, 1)/2$
		$a(0, 0, \pm 1)/2$			$\pm a(1, 1, 0)/2$
					$\pm a(0, 1, -1)/2$
					$\pm a(1, 0, -1)/2$
					$\pm a(1, -1, 0)/2$
A	B	$a(1, -1, -1)/4$	A'	B	$a(-1, 1, 1)/4$
B	A'	$a(-1, -1, 1)/4$	B	A	$a(1, 1, -1)/4$
		$a(-1, 1, -1)/4$			$a(1, -1, 1)/4$
		$a(1, 1, 1)/4$			$a(-1, -1, -1)/4$

on the different sublattices of Mg_2X in table 1. To further simplify our notation, we have defined $\alpha, \beta \in \{A, A', B\}$. Although, throughout the paper, we shall discuss the model constructed and results obtained by the nearest-neighbor interactions, we have constructed models incorporating both the nearest-neighbor and next nearest-neighbor interactions simultaneously. Our results revealed only a slight improvement and therefore we avoid presenting the models with the next nearest-neighbor interactions.

3. Multi-orbital tight-binding model

When isolated atoms are brought together to form a material, the individual atomic orbitals of each atom start interacting with those of neighboring atoms. This interaction is largest among electrons that occupy the outer electron shells and diminishes among electrons within inner electron shells. The interactions can be bonding or anti-bonding and therefore, the molecular orbitals that describe the physical properties of a material can be a combination of the original atomic orbitals. To construct a reliable model Hamiltonian that contains these pivotal aspects, the interaction among the electrons, occupying

the outer electron shells, should be properly accounted for. In this case, the Hamiltonian can be expressed by:

$$\hat{\mathcal{H}} = \sum_{\mathbf{k}, \mu\nu, \alpha\beta, \sigma\sigma'} \left\{ \mathcal{E}_{\mu\nu, \sigma\sigma'}^{\alpha\beta} \delta_{\alpha\beta} \delta_{\mu\nu} \delta_{\sigma\sigma'} + \gamma_{\mu\nu, \sigma\sigma'}^{\alpha\beta}(\mathbf{k}) \delta_{\sigma\sigma'} + \eta_{\mu\nu, \sigma\sigma'}^{\alpha\beta} \delta_{\alpha\beta} \right\} C_{\mu\nu, \sigma\sigma'}^{\alpha\beta\dagger} C_{\mu\nu, \sigma\sigma'}^{\alpha\beta} + \text{h.c.}, \quad (1)$$

where the on-site energy, hopping integrals among atoms, and SOI are denoted by \mathcal{E} , γ , and η , respectively. The different atoms are marked by α, β whereas μ, ν and σ, σ' represent the electron orbitals and spin species, respectively, $C_{\mu\nu, \sigma\sigma'}^{\alpha\beta(\dagger)}$ is the annihilation (creation) operator and δ_{ij} is the Kronecker delta function. By the inclusion of multi-orbital interactions among different atoms, electrons can occupy mixed and intermediate states with some finite probability. The multi-orbital nature of our TB Hamiltonian is encoded into the hopping integrals as follows:

$$\gamma_{\mu\nu}^{\alpha\beta}(\mathbf{k}) \equiv \sum_{\delta \in \delta_{\alpha\beta}} t_{\mu\nu}^{\alpha\beta}(\delta) \exp(i\mathbf{k} \cdot \delta), \quad (2)$$

in which \mathbf{k} is the momentum of a particular moving electron, δ is the displacement vector, and $t_{\mu\nu}^{\alpha\beta}(\delta)$ is the hopping integrals [40].

Because of stronger interactions in heavy elements, the spin-orbital mediated interactions play an important role and considerably change the properties of a material [41]. The intrinsic SOI in a crystal can generally be given by [41]:

$$\mathcal{H}_{\text{SO}} = \zeta(r) \hat{\mathbf{L}} \cdot \hat{\mathbf{S}}, \quad (3a)$$

$$\zeta(r) \propto \frac{1}{r} \frac{\partial V(r)}{\partial r}, \quad (3b)$$

where \mathbf{L} and \mathbf{S} are the total orbital and spin angular momentum operators, respectively, and $V(r)$ is the total crystal potential. In this model, $\zeta(r)$ depends both on position r and the crystal potential, and therefore deals with the radial part $R_{n,l}(r)$ of the electron-orbital wave functions $\Psi_{n,l,m}$, which are dependent on quantum numbers n and l through:

$$\Psi_{n,l,m} = R_{n,l}(r) Y_{l,m}(\theta, \phi). \quad (4)$$

Therefore, the spin-orbit coupled part of the Hamiltonian equation (1) in its component form can be expressed by:

$$\eta_{\mu\nu, \sigma\sigma'} = \eta_{\text{SO}} \langle \hat{\mathbf{L}} \cdot \hat{\mathbf{S}} \rangle_{\mu\nu, \sigma\sigma'}. \quad (5)$$

To evaluate equation (5), it is more convenient to introduce the ladder SOI operators as follows:

$$\begin{aligned} \hat{\mathbf{L}} \cdot \hat{\mathbf{S}} &= \hat{L}_z \hat{S}_z + \frac{1}{2} (\hat{L}_+ \hat{S}_- + \hat{L}_- \hat{S}_+), \\ \hat{L}_{\pm} &= \hat{L}_x \pm i \hat{L}_y, \\ \hat{S}_{\pm} &= \hat{S}_x \pm i \hat{S}_y. \end{aligned} \quad (6)$$

Defining n, l, m, s as the principal, azimuthal, magnetic, and spin quantum numbers, respectively, the quantum numbers are restricted by $l = \{0, 1, 2, \dots, n-1\}$, $m = \{-l, -l+1, \dots,$

$l-1, l\}$, and $s = \pm 1/2$. The operation of the angular and spin operators on a wave function at a state $\psi_{l,m,s}$ are summarized as follows:

$$\begin{aligned}\hat{S}_z \psi_{l,m,s} &= s \psi_{l,m,s}, \\ \hat{L}_z \psi_{l,m,s} &= m \psi_{l,m,s}, \\ \hat{L}_{\pm} \psi_{l,m,s} &= \sqrt{(l \mp m)(l \pm m + 1)} \psi_{l,m \pm 1,s}, \\ \hat{S}_{\pm} \psi_{l,m,\pm 1/2} &= 0, \\ \hat{S}_{\pm} \psi_{l,m,\mp 1/2} &= \psi_{l,m,\pm 1/2}, \\ \hat{L}_z \hat{S}_z \psi_{l,m,s} &= m s \psi_{l,m,s}, \\ \hat{L}_{\pm} \hat{S}_{\mp} \psi_{l,m,\pm 1/2} &= \frac{1}{2} \sqrt{(l-m)(l+m+1)} \psi_{l,m \pm 1,\mp 1/2}.\end{aligned}\quad (7)$$

Further details on the inclusion of SOI in the formalism is presented appendix A (see equation (A28)). In the equations above, we have set $\hbar = 1$ to simplify the notation.

Since the inner shell electrons are strongly bonded to nuclei, one can consider them as frozen electrons and only account for the interaction among the valence shell electrons. Therefore, we have constructed several models, accounting for excited electrons up into the d orbitals, i.e. $\{d_{xy}, d_{yz}, d_{zx}, d_{x^2-y^2}, d_{3z^2-r^2}\}$. For example, in the smallest model where it describes five electronic bands around the Fermi level, we consider the interaction among $\{s, p_x, p_y, p_z\}$ orbitals. In the largest model, the interaction among $\{s, p_x, p_y, p_z, d_{xy}, d_{yz}, d_{zx}, d_{x^2-y^2}, d_{3z^2-r^2}, s^*\}$ orbitals are considered and the model is able to describe eighteen electronic bands around the Fermi level. These interactions result in relatively large expressions for the hopping integrals that are given in appendix A.

4. Machine-learning for finding optimized parameters to the TB models

As described in the previous section and given in appendix A, the TB models in the presence of SOI can contain tens of unknown parameters to be calibrated through comparison with a reference data set (in our case, the DFT data of the band structure is the reference). Therefore, one needs an efficient approach to find optimal and reliable parameter values to the TB models. One efficient machine-learning approach is the simulated annealing (SA), which is a Monte-Carlo method for derivative-free optimization, built on concepts from statistical physics [42]. The SA algorithm mimics the annealing process by first defining some cost function. Next, an initially high temperature T is simulated by allowing the coordinates of the system to randomly fluctuate. Thermal equilibrium is gradually achieved by slowly cooling the system and primarily allowing fluctuations that decrease the cost-function. Fluctuations that increase the cost-function are accepted with probability $h(\Delta C)$. In our optimization process, we have defined a cost function:

$$\begin{aligned}\mathbb{C}(\mathcal{E}) &= \sqrt{\frac{1}{M} \sum_i w_i (\mathcal{E}_i - \mathcal{E}_i^r)^2}, \\ M &= \sum_i w_i.\end{aligned}\quad (8)$$

In equation (8), the sum runs both over all the data-points of the model and the corresponding reference data points \mathcal{E}_i^r . Depending on the problem, the weight distribution can be set to $w_i = 1$. Oftentimes, a nonuniform weight distribution, such as increased weights for bands closer to the Fermi energy, is appropriate for problems where the deviation among the data points and reference data points is considerably large and produces outliers. The acceptance criterion of a set of parameter values is used as follows:

$$h(\Delta C) = \frac{1}{1 + \exp(\Delta C/T)} \approx \exp(-\Delta C/T). \quad (9)$$

The variation of \mathbb{C} between two steps is shown by ΔC . The cooling schedule for a given parameter α^i is:

$$T(t) = T_0 \exp(-ct^{1/d}), \quad (10)$$

where T_0 is the initial temperature, d is the (effective) dimension of parameter space, and c is a tunable cooling constant. To incorporate the temperature schedule, i.e. equation (10), the update to each parameter α^i :

$$\alpha_{t+1}^i = \alpha_t^i + y^i (\mathbb{B}_i - \mathbb{A}_i), \quad (11)$$

are drawn from the distribution:

$$\begin{aligned}y^i &= \text{sgn}\left(u^i - \frac{1}{2}\right) T(t_i) [(1 + T(t_i)^{-1})^{|2u^i-1|} - 1], \\ u^i &= U[0, 1],\end{aligned}\quad (12)$$

where sgn is the sign function, $T(t_i)$ is the temperature of parameter α^i at step i , and $U[0, 1]$ is the continuous uniform distribution between 0 and 1. Also, \mathbb{B}_i and \mathbb{A}_i are the upper and lower boundaries for the search space of parameter α^i . The random generator (12) always produces a number in the range $[-1, 1]$. The full span of the search space for each parameter $\mathbb{B}_i - \mathbb{A}_i$ is not necessarily known, but may be approximated to bias the algorithm towards generating step sizes proportional to the relevant search space. Fluctuations in more sensitive parameters cause more significant changes to the cost function. One can efficiently optimize values to the more sensitive and the less sensitive parameters by multiple rounds of the annealing process, where more (less) sensitive parameters are gradually allowed to fluctuate relatively less (more). This re-annealing strategy was suggested by Ingber and Rosen [43] where the less sensitive parameters are periodically re-annealed as follows:

$$\begin{aligned}t \leftarrow t'_i &= \max\left[0, \left(\frac{1}{c} \ln\left(\frac{T_0}{T(t_i)} \frac{s_i}{s_{\max}}\right)\right)^d\right], \\ s_i &= (\mathbb{B}_i - \mathbb{A}_i) \frac{\partial \mathbb{C}(\alpha)}{\partial \alpha^i} \\ &\approx (\mathbb{B}_i - \mathbb{A}_i) \frac{\mathbb{C}([\alpha^1, \dots, \alpha^i + \delta\alpha, \dots, \alpha^d]) - \mathbb{C}(\alpha)}{\delta\alpha}.\end{aligned}\quad (13)$$

Here, s_i is the sensitivity of parameter α^i , s_{\max} is the largest sensitivity, $\delta\alpha$ is a small increment in one parameter and α is the vector of parameters.

The required extensive search of the high-dimensional parameter space of our TB models using the Monte-Carlo algorithm is a slow process, especially when many different datasets are to be considered. To speed up our extensive search to find best optimized TB parameters, we have implemented a massively parallelized algorithm using graphical processing units.

5. First-principles density functional theory calculations

The DFT calculations of electronic structure are performed using the GPAW package [44]. We have employed the gradient-corrected PBE approximation for the exchange-correlation energy functional. The \mathbf{k} space grid is constructed by the Monkhorst–Pack scheme and a relatively large value of grid density is used, i.e. 8.0 \mathbf{k} -points per 1 \AA^{-1} . The kinetic energy cutoff for plane waves is set to 800 eV. The width of the Fermi–Dirac distribution is set to 0.01 eV. All DFT calculations presented are performed in the presence of SOI. Also, the results from DFT without SOI are used for investigating the influence of SOI on the band-structure.

To simulate the strained configurations, we introduce a strain tensor with components ε_{ij} in which the indices run over real space coordinations, i.e. $ij \in x, y, z$. The strained unit cell and therefore updated locations of the different atoms can be described by the new vectors: $a = \varepsilon_{xx}a_0$, $b = \varepsilon_{yy}b_0$, and $c = \varepsilon_{zz}c_0$. The unstrained vectors are a_0 , b_0 , and c_0 . In what follows, we restrict our simulations to a low-strain regime, i.e. $\pm 10\%$ to make sure no structural transition occurs upon inserting strain into the unit cell. In order to determine any structural transition, one has to perform high-throughput calculations and span a huge search space made of various structures. Nevertheless, from previous studies on two-dimensional materials (see [45] and references therein), which are more sensitive to strain, we assume that the antiferroite Mg_2X compounds with a cubic-like configuration are stable in the presence of strain less than $\pm 10\%$. Note that $\pm 10\%$ of strain corresponds to 10% of tensile and compressive strain, respectively. Throughout the paper, we consider uniform strain in all directions.

The radii of X elements differ considerably. Therefore, one can expect that the lattice constants of Mg_2X compositions vary significantly. In order to find the energetically stable lattice constant for each composition, we have performed DFT calculations and plotted the formation energy of these compounds as a function of lattice constant a in figure 2. The formation energy is normalized by the number of atoms in the unit cell. As seen, Mg_2Si has the smallest lattice constant, i.e. $a_0 = 6.362 \text{ \AA}$ whereas the lattice constant of Mg_2Pb is largest: $a_0 = 6.908 \text{ \AA}$. The predicted lattice constants for the compounds Mg_2Ge and Mg_2Sn are $a_0 = 6.426, 6.807 \text{ \AA}$, respectively. These results are perfectly aligned with the increase of atomic numbers and radius of atoms among Si, Ge, Sn, Pb. The obtained lattice constants are in good agreement with experiments as summarized in table 2 [46–48]. In the calculations and discussions that follow, we shall use the above predicted lattice constants for the relaxed structures in the absence of

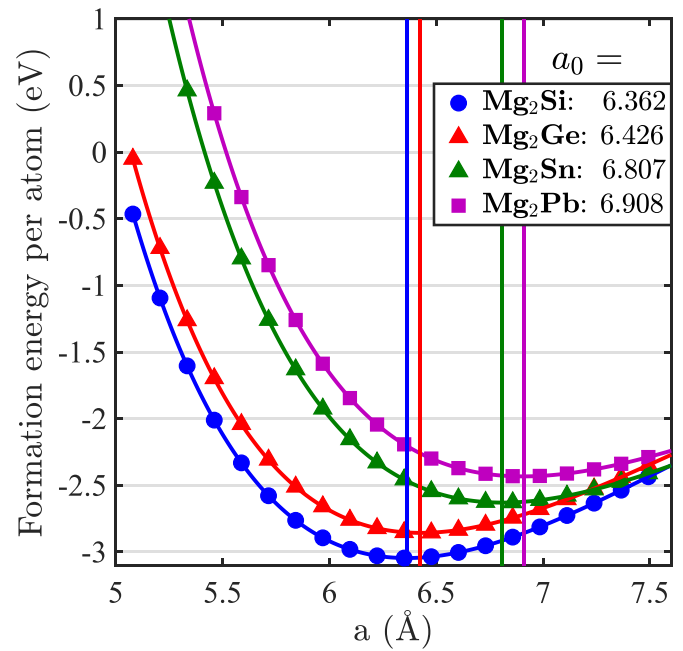


Figure 2. The DFT formation energy per atom as a function of lattice parameter a for the different compounds of Mg_2X ($\text{X} = \text{Si}, \text{Ge}, \text{Sn}, \text{Pb}$). The energetically favorable lattice constants are obtained as $a_0 = 6.362, 6.426, 6.807, 6.908 \text{ \AA}$, respectively. The vertical lines exhibit the location of the optimized lattice constants.

Table 2. The lattice constant of Mg_2X from experiment and DFT predictions.

Compound	Experiment a_0 (Å)	DFT a_0 (Å)
Mg_2Si	6.340	6.362
Mg_2Ge	6.385	6.426
Mg_2Sn	6.765	6.807
Mg_2Pb	6.836	6.908

strain and obtain strained structures accordingly. Therefore, the normalized formation energy of the strained structures can be found in figure 2 as well.

6. Results and discussions

In section 6.1 we discuss the band structure results of the five-band TB model. The contribution of the s and p orbitals of Mg and X to the total band structure is discussed in section 6.2. The strength of SOI and the σ and π bondings in Mg_2X are presented in sections 6.3 and 6.4, respectively.

6.1. The band structure from the machine-learned five-band TB model

Figure 3 exhibits the band structure of Mg_2X ($\text{X} = \text{Si}, \text{Ge}, \text{Sn}, \text{Pb}$). In all cases, the Fermi level is shifted to zero energy. The dashed red curves are obtained through DFT whereas the solid blue curves are the results of our machine-learned five-band TB model. Column-wise, the element X

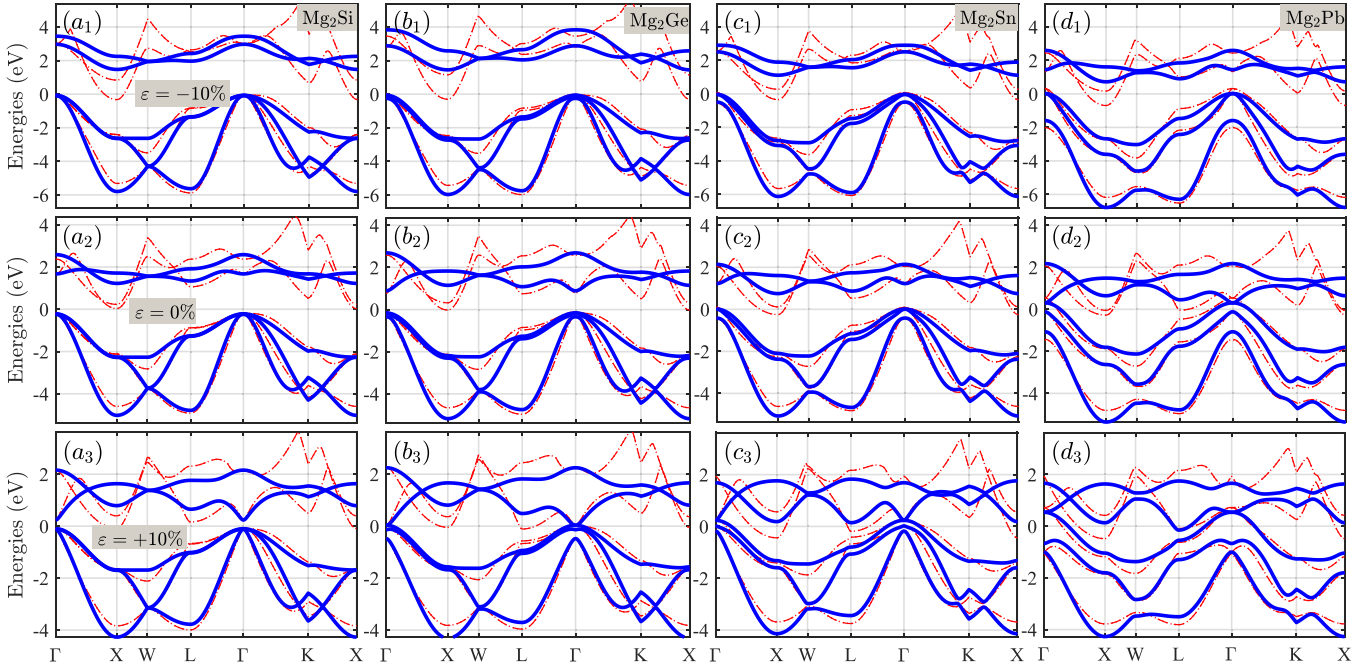


Figure 3. The band structure of Mg_2X along a high-symmetry path $\Gamma\text{XWL}\Gamma\text{KX}$. Column-wise, from left to right, the element $\text{X} = \text{Si}, \text{Ge}, \text{Sn}, \text{Pb}$ changes, respectively. Row-wise, the applied strain varies $\varepsilon = -10\%, 0\%, +10\%$ from top to bottom, respectively. The dashed curves show DFT predictions and the solid curves are the results of the machine-learned five-band TB model.

changes as $\text{X} = \text{Si}, \text{Ge}, \text{Sn}, \text{Pb}$ from left to right, respectively. Row-wise, figure 3 shows how strain affects the band structure at $\varepsilon = -10\%, 0\%, +10\%$ from top to bottom, respectively. The band structure is plotted along the high-symmetry path $\Gamma\text{XWL}\Gamma\text{KX}$ in \mathbf{k} -space. As seen, our five-band TB model reproduces the band structures in a good agreement to the DFT results. Specifically, the three valence bands produced by the five-band TB model deviate only slightly from those of DFT. Similarly, the same precision in predicting the valence bands is accessible to larger models than the five-band model. The two conduction bands, however, have larger deviations from those of DFT although at the Γ point we yet see good agreement between the model prediction and DFT. The main reason for the larger deviation of the conduction bands originates from the exclusion of higher excited states in our five-band TB model. In fact, an excited mode over the Fermi level is a complicated hybridization of several excited states. However, in the five-band TB model, we have considered the contribution of five orbitals only, namely the $3s$ orbital of Mg and the $\{p_x, p_y, p_z\}$ orbitals of the X elements. Therefore, in order to obtain more accurate predictions for the conduction bands using the TB method, one needs to take more of the excited orbitals into account. To confirm this, we have considered the $\{3s, 3p\}$ orbitals of Mg and $\{s, p, d, s^*\}$ orbitals of X, constructed an eighteen-band TB model, and calibrated the model to the DFT band structures. The results revealed almost perfect reproduction of the band structures obtained by DFT, close to the Fermi level. A representative band structure from the machine-learned eighteen-band TB model is shown in figure 7 of appendix B. As seen, most of the band features and details of DFT are now reproduced with the larger TB model. Therefore, the five-band model supports the valence bands accurately

and, compared to the single-band parabolic model, it captures the curvature of the valence/conduction bands at the γ point. Depending on the required accuracy within the conduction bands, one can employ either of the five-band or eighteen-band models at the cost of computational speed. In the following, the s orbital of Mg and the p orbitals of X is equivalent to the $3s$ orbital of Mg, and $3p$ orbitals of Si, $4p$ orbitals of Ge, $5p$ orbitals of Sn, and $6p$ orbitals of Pb, respectively.

6.2. The contribution of s and p orbitals

The obtained parameter values of the five-band TB model for $\varepsilon = 0\%, \pm 10\%$ are given in appendix C. Our five-band TB model is able to describe the low-energy properties of the compounds Mg_2X , e.g. through projection of the total band structure onto different orbitals. Figure 4 illustrates the projection of the total band structure of Mg_2Ge onto each orbital. The analysis of the Mg_2X compounds showed that these orbitals play similar roles in them. Therefore, we discuss the representative case of Mg_2Ge . Figures 4(a), 4(b), and 4(c) illustrate how strains of $\varepsilon = -10\%, 0\%, +10\%$, respectively, influence the contribution of the individual orbitals to the total band structure. For visualization reasons, the contribution of the bands is proportional to their thickness, i.e. the thicker parts have larger contribution than the thinner segments. Figures 4(a₁), 4(b₁), and 4(c₁) display the contribution of the s orbital of Mg whereas the contributions of the $\{p_x, p_y, p_z\}$ orbitals of Sn are shown in figures 4(a₂, b₂, c₂), 4(a₃, b₃, c₃), and 4(a₄, b₄, c₄), respectively.

First, the figures illustrate that the contribution of the s orbital of Mg is largest to the conduction bands whereas the p orbitals of X have the largest contribution to the valence bands.

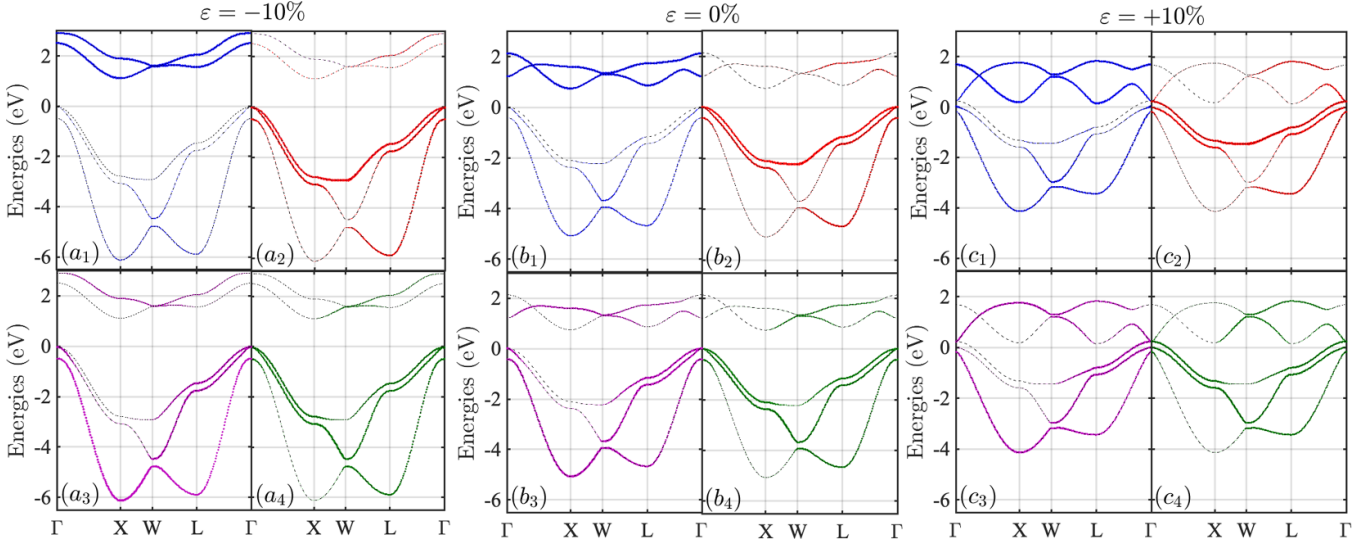


Figure 4. The projection of the total band structure onto the $\{s, p_x, p_y, p_z\}$ orbitals. The applied uniform strain to the system is $\varepsilon = -10\%, 0\%, +10\%$ in panels with (a)–(c) labels, respectively. The panels with index ‘1’ show the contribution of the 3s orbital of Mg whereas the panels with indices ‘2’, ‘3’, and ‘4’ display the contribution of the $5p_x, 5p_y, 5p_z$ orbitals of Sn, respectively.

Therefore, in a compound Mg_2X , the energy of particles occupying the s orbital of Mg is larger than those occupying the p orbitals of X. The analysis of twelve-band and eighteen-band TB models showed that the energy of particles occupying the s orbital of X is lower than its p orbitals and thus has no contribution to the orbitals of our five-band TB model. It was found that the p orbitals of Mg and d orbitals of X contribute slightly to the total valence band as well, but much less significant than the s orbital of Mg and p orbitals of X. It is well understood that the excited particles are basically governed by the conduction bands. Hence, figure 4 reveals the fact that when the two elements Mg and X are brought together in the antifluorite configuration shown in figure 1, Mg tends to transfer its two s electrons to the p orbitals of X. Therefore, in the Mg_2X ($\text{X} = \text{Si}, \text{Ge}, \text{Sn}, \text{Pb}$) compounds considered here, Mg plays a cation role whereas X turns into an anion and create $\text{Mg}_2^{2+}\text{X}^{4-}$, which is consistent with the electronegativity scale.

Second, figure 3 shows that the main contribution to the valence band structure and accordingly, the main physical properties of Mg_2X at equilibrium originate from the p orbitals of the X atoms. Thus, to account for SOI in our five-band TB model, one can simply include the spin–orbit mediated interactions among the p particles only.

A compressive strain on the order of $\varepsilon = -10\%$, shown in the leftmost panels of figure 4, weakens the contribution of the s orbital of Mg (figure 4(a₁)) and causes a dominant contribution of the p orbitals of X to the valence bands. Subject to $\varepsilon = -10\%$ of strain, the contribution of the p orbitals of X to the conduction bands is negligible while the s orbital of Mg governs the conduction bands. The application of $\varepsilon = +10\%$ tensile strain, however, has an exact reversed effect and causes more contribution of the s orbital of Mg and p orbitals of X to the valence and conduction bands, respectively. These features

can be fully understood by noting the fact that compressive and tensile strains result in stronger and weaker coupling of the orbitals, respectively. Therefore, in the presence of $\varepsilon = -10\%$ strain, the s orbital of Mg acquires stronger contribution to the conduction bands and becomes energetically less favorable (appears at larger positive energies when comparing the conduction bands of figures 4(a₁)–(b₁)). Whereas the contribution of the p orbitals of X to the total band structure is more localized on the valence bands. This can be confirmed when comparing figures 4(a₂, a₃, a₄) with figures 4(b₂, b₃, b₄)) where the p orbitals of X become energetically more favorable (appear at larger negative energies). In contrast, when subject to $+10\%$ of tensile strain, the Mg and X atoms are slightly decoupled and therefore the entire system tends to acquire properties closer to isolated atomic species. This is clearly seen in figures 4(c) that not only the contribution of the s orbital of Mg to the valence bands is strengthened but the conduction bands also acquire smaller positive energies. Likewise, the p orbitals of X acquire smaller negative energies. The results of our five-band TB model for the orbital contributions in unstrained Mg_2X are in agreement with those concluded from DFT [15, 49, 50].

6.3. Strength of spin–orbit interaction

As pointed out earlier, the TB model allows us to estimate the strength of SOI in the Mg_2X compounds. Utilizing our machine-learned five-band TB model, we have summarized the strength of SOI, η_{SO} , for $\text{X} = \text{Si}, \text{Ge}, \text{Sn}, \text{Pb}$ and strain values from $\varepsilon = -10\%$ to $\varepsilon = +10\%$ by a step of 2% in table 3. To obtain the results of η_{SO} in table 3, we have confined our model to a small interval around the Γ point. This confinement results in a perfect fit to the DFT band structure and more accurate estimation of η_{SO} . Also, we have summarized the values of η_{SO} by fitting the five-band TB model to the entire Brillouin

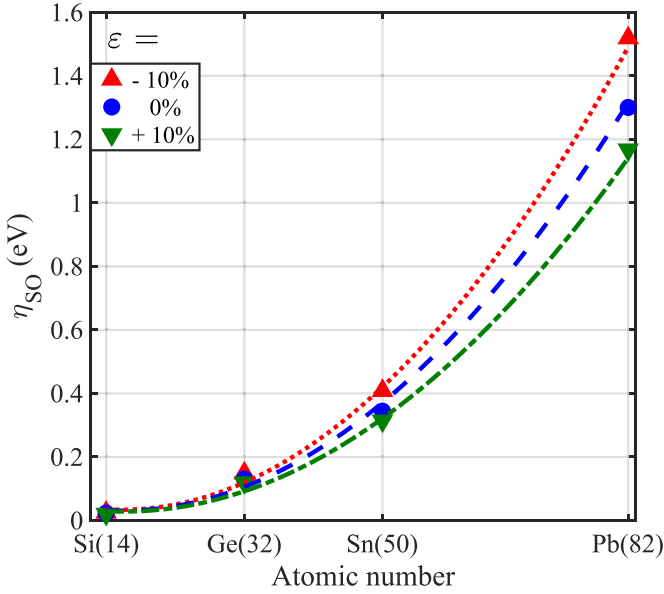


Figure 5. The strength of spin–orbit interaction as a function of the atomic number of the elements $X = \text{Si, Ge, Sn, Pb}$. The maximum compressive and tensile strain values are applied to the system, i.e. $\varepsilon = \pm 10\%$ and compared with the cases without any strain, i.e. $\varepsilon = 0\%$.

zone in appendix C. Nevertheless, the physical trends and conclusions made remain the same. We have shown the values of η_{SO} , obtained through the confined five-band TB model, as a function of $X = \text{Si, Ge, Sn, Pb}$ for $\varepsilon = 0\%, \pm 10\%$ by dots in figure 5. As seen, the strength of SOI follows a significant and systematic enhancement by increasing the atomic number z of X . We tested several functions, including exponential and polynomial ones, to determine the functionality of η_{SO} to z and ε . Our results suggested a second order polynomial as a function of z with a least deviation from the original data points as follows:

$$\eta_{\text{SO}}(\varepsilon, z) = \mathcal{A}(\varepsilon)z^2 + \mathcal{B}(\varepsilon)z + \mathcal{C}(\varepsilon). \quad (14)$$

Further investigations found that the coefficients of the polynomial function possess linear functionalities with respect to strain ε so that the coefficients can be described by:

$$\begin{aligned} \mathcal{A}(\varepsilon) &= \mathcal{A}_1\varepsilon + \mathcal{A}_2, \\ \mathcal{B}(\varepsilon) &= \mathcal{B}_1\varepsilon + \mathcal{B}_2, \\ \mathcal{C}(\varepsilon) &= \mathcal{C}_1\varepsilon + \mathcal{C}_2, \end{aligned} \quad (15)$$

in which the constant values are $\mathcal{A}_1 = -0.385$ meV, $\mathcal{A}_2 = 0.681$ meV, $\mathcal{B}_1 = 11.7$ meV, $\mathcal{B}_2 = -2.12$ meV, $\mathcal{C}_1 = -115.5$ meV, $\mathcal{C}_2 = 223.3$ meV. Therefore, equations (14) and (15) determine the dependence of the strength of SOI to the atomic number of X and strain ε . To illustrate the efficiency of this model, we have plotted $\eta_{\text{SO}}(\varepsilon, z)$ as a function of z and three values of strain by dashed lines in figure 5. We see that the obtained equation (14) can properly predict the variation of

SOI in Mg_2X subject to strain. Figure 5 and table 3 demonstrate that compressive and tensile strains enhance and suppress η_{SO} , respectively. This is consistent with the contribution of the p orbitals of X to the total band structure found in figure 4.

According to the findings of thermoelectric effects reported in the literature and discussed earlier in Introduction, the delicate splitting and aspects of the band structure highly influence the Seebeck coefficient, charge conductance, and phonon scattering. The latter quantities determine the thermoelectric power of a material. Therefore, our results of the band structure upon changing X and exerting strain point into the fundamentally important ingredients to be accounted for when analyzing various physical properties of Mg_2X . Note that, in general, the unstrained Mg_2X compounds are indirect band gap semiconductors [34] and we here instead focus on the valence band splittings. The detailed study on the indirect band gaps of the Mg_2X compounds subject to strain can be the focus of a future work.

The three valence bands in the total band structure are degenerate at the Γ point for some cases as seen in figure 3. These three bands however split into two and three bands at the Γ point as a result of SOI, depending on strain and the atomic number of X . The results are summarized in table 3. The highest valence band at the Γ point is labeled by 1st and the first and second bands below the highest valence band are named 2nd and 3rd bands, respectively. The splitting magnitudes between 1st–2nd and 1st–3rd are denoted by $g_{\varepsilon, \text{SO}}^1$ and $g_{\varepsilon, \text{SO}}^2$, respectively. The $g_{\varepsilon, \text{SO}}^1$ band splitting at the Γ point in Mg_2Si is zero throughout the entire strain interval we considered. However, $g_{\varepsilon, \text{SO}}^1$ acquires nonzero values when applying $\varepsilon > 5\%$ of tensile strain to Mg_2Ge . The splitting increases in Mg_2Sn and Mg_2Pb and appears even at compressive strains. This is in contrast to $g_{\varepsilon, \text{SO}}^2$, which is nonzero for all compounds and enhances (suppresses) in the presence of compressive (tensile) strain similar to the strength of SOI. Note that the values of the band splittings $g_{\varepsilon, \text{SO}}^2$ are different from the strength of SOI, η_{SO} .

6.4. The contribution of σ and π bondings

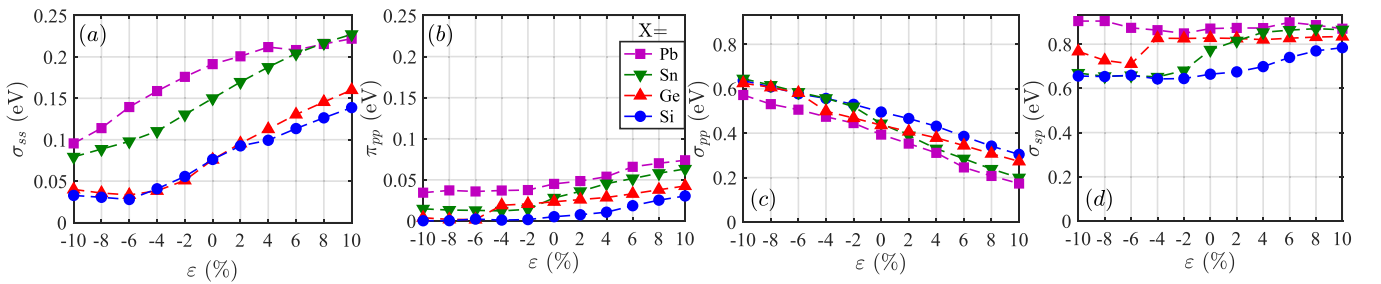
The five-band TB model further provides insightful information into the type of bondings and their strength in the Mg_2X compounds. We have extracted the behavior of the σ bondings and π bonding energies from our model and plotted them as a function of strain for different X in figure 6. Also, the exact values of the bonding parameters are given in appendix C. The σ bondings among s - s orbitals, p - p orbitals, and s - p orbitals are shown by σ_{ss} , σ_{pp} , and σ_{sp} , respectively, while the π bonding among the p - p orbitals is denoted by π_{pp} . The results in figure 6(b) reveal that the π_{pp} bonding is negligible compared with the σ bondings shown in figures 6(a), (c) and (d). The largest variation upon strain belongs to σ_{pp} and compressive strain enhances σ_{pp} . Also, figures 6(c) and (d) show that σ_{sp} and σ_{pp} are the dominating bondings in Mg_2X .

Table 3. The strength of SOI, η_{SO} , and band splittings $g_{\varepsilon,\text{SO}}^1$ and $g_{\varepsilon,\text{SO}}^2$ at the Γ point in the Mg_2X ($\text{X} = \text{Si}, \text{Ge}, \text{Sn}, \text{Pb}$) compounds subject to strain $\varepsilon \in [-10\%, +10\%]$.

The strength of spin–orbit interaction from the five band TB model η_{SO} (meV)											
ε	−10%	−8%	−6%	−4%	−2%	0%	+2%	+4%	+6%	+8%	+10%
Mg_2Si	25.4	24.7	24.0	23.6	23.2	23.0	22.7	21.3	21.0	20.6	20.4
Mg_2Ge	149.1	144.8	141.0	136.9	133.5	130.5	127.9	125.7	124.3	121.8	119.7
Mg_2Sn	408.7	394.3	379.9	368.3	355.9	344.1	332.2	321.2	320.9	316.5	314
Mg_2Pb	1519.0	1475.9	1425.5	1376.4	1335.6	1300.5	1269.2	1241.6	1216.6	1193.8	1167.5

The band splitting between 1st and 2nd valence bands at the Γ point $g_{\varepsilon,\text{SO}}^1$ (meV)											
Mg_2Si	0.0	0.0	0.0	0.0	0.0	0.0	0.0	0.0	0.0	0.0	0.0
Mg_2Ge	0.0	0.0	0.0	0.0	0.0	0.0	0.0	0.0	16.8	182.6	179.7
Mg_2Sn	0.0	0.0	0.0	0.0	0.2	0.3	0.5	0.9	1.0	20.1	265.2
Mg_2Pb	0.0	0.0	0.3	18.1	316.6	592.0	855.0	1097.1	1318.7	1519.5	1699.5

The band splitting between 1st and 3rd valence bands at the Γ point $g_{\varepsilon,\text{SO}}^2$ (meV)											
Mg_2Si	37.5	36.4	35.4	34.5	33.6	32.9	32.2	31.5	30.9	30.4	29.9
Mg_2Ge	226.2	219.8	213.6	207.9	202.6	197.8	193.4	189.4	185.8	276.5	515.4
Mg_2Sn	622.8	600.8	580.5	561.9	545.1	529.1	516.7	504.9	493.8	482.1	471.6
Mg_2Pb	2334.5	2247.0	2166.4	2093.1	2029.8	1973.3	1918.9	1871.9	1822.3	1778.2	1748.3

**Figure 6.** The absolute values of bondings $\sigma_{ss}, \pi_{pp}, \sigma_{pp}, \sigma_{sp}$, as a function of strain ε , are displayed in panels (a)–(d), respectively. The curves with different symbols show the different compounds Mg_2X ($\text{X} = \text{Si}, \text{Ge}, \text{Sn}, \text{Pb}$).

7. Conclusions

We have developed machine-learned MMTB model Hamiltonians to study the electronic properties of the Mg_2X ($\text{X} = \text{Si}, \text{Ge}, \text{Sn}, \text{Pb}$) antifluorite structures subject to uniform strain. The MMTB models are fitted to the DFT band structure using a massively parallelized Monte-Carlo search algorithm. The investigations demonstrate that a machine-learned five-band TB model, accounting for the s orbital of Mg and $\{p_x, p_y, p_z\}$ orbitals of X occupying their outer electron shells, respectively, can sufficiently describe the electronic characteristics of Mg_2X close to the Fermi level, in particular, the valence band and the effect of SOI. We find that the Mg atoms tend to transfer their electrons, occupying the s orbital, to the p orbitals of the X atoms and create $\text{Mg}_2^{2+}\text{X}^{4-}$. This phenomenon is clearly seen in the projected band structure where the s orbital of Mg is largest on the conduction bands, supporting excited states, whereas the contribution of the p orbitals of X is largest on the valence bands with energies lower than the Fermi level. The application of compressive strain causes further localization of the contribution of the s orbital of Mg to

the conduction bands at higher energies above the Fermi level and the p orbitals of X to the valence bands at lower energies below the Fermi level. Tensile strain, however, has a reversed effect and weakens the contributions of the s orbital of Mg and the p orbitals of X to the conduction bands and valence bands, respectively.

The analysis of the projected band structures shows that the SOI in Mg_2X originates from the p orbitals of X. Extracting the strength of SOI η_{SO} through the five-band TB model, we have obtained a function for predicting η_{SO} in the presence of strain and against the atomic number of X. The five-band TB model reveals that the main bonding contributions in the Mg_2X compounds are $|\sigma_{sp}| > |\sigma_{pp}| > |\sigma_{ss}|$, and that the π bonding is negligible. σ_{pp} shows the largest variation upon applying strain.

We have found that both X and strain can effectively control the band gap of Mg_2X , turning a semiconductor into metal and vice versa, and efficiently manipulate the band splitting of the valence bands at the Γ point. These findings point into controllable electronic properties, quantum transport, and thermoelectric effects in these materials. Our five-band TB

model can be generalized and utilized to study large-scale Mg_2X -based compounds both in molecular dynamics simulations and quantum transport studies with more accuracy compared to those of single-band parabolic models available in the literature. Moreover, the presented TB construction approach which combines DFT band structure with multi-dimensional Monte-Carlo search of parameters can be applied to a wide variety of materials.

Data availability statement

All data that support the findings of this study are included within the article (and any supplementary files).

Acknowledgments

The DFT calculations were performed using the resources provided by UNINETT Sigma2-the National Infrastructure for High Performance Computing and Data Storage in Norway, Project Number: NN9497K. Financial support from the NTNU Digital Transformation program (Norway) for the project ALLDESIGN is gratefully acknowledged.

Appendix A. Hopping integrals and SOI matrix elements for the eighteen-band TB model

In this appendix, we present the components of the largest TB model constructed. This model includes $\{s, p_x, p_y, p_z, d_{xy}, d_{yz}, d_{zx}, d_{x^2-y^2}, d_{3z^2-r^2}, s^*\}$ orbitals and describes eighteen electronic bands around the Fermi level. To construct smaller models, similar to the five-band TB model presented in the main text, one simply needs to remove the associated interactions in the eighteen-band TB model. The basis set for the largest TB model is given by:

$$\Psi_{18} = \left(C_{s\sigma}^A, C_{p_x\sigma}^A, C_{p_y\sigma}^A, C_{p_z\sigma}^A, C_{s\sigma}^{A'}, C_{p_x\sigma}^{A'}, C_{p_y\sigma}^{A'}, C_{p_z\sigma}^{A'}, C_{s\sigma}^B, C_{p_x\sigma}^B, C_{p_y\sigma}^B, C_{p_z\sigma}^B, C_{d_{xy}\sigma}^B, C_{d_{yz}\sigma}^B, C_{d_{zx}\sigma}^B, C_{d_{x^2-y^2}\sigma}^B, C_{d_{3z^2-r^2}\sigma}^B, C_{s^*\sigma}^B \right)^T. \quad (\text{A1})$$

The basis set used in the five-band model is instead:

$$\Psi_5 = \left(C_{s\sigma}^A, C_{s\sigma}^{A'}, C_{p_x\sigma}^B, C_{p_y\sigma}^B, C_{p_z\sigma}^B \right)^T. \quad (\text{A2})$$

In the following, we have summarized the various interactions and hopping integrals in matrices that arise in our largest TB model:

$$\gamma(\mathbf{k}) = \begin{pmatrix} \mu & A_s & A_p & A'_s & A'_p & B_s & B_p & B_d & B_s^* \\ A_s & & & & & & & \gamma_{sd}^{AB} [1 \times 5] & \gamma_{s^*s}^{AB} \\ A_p & & & & & & & \gamma_{pd}^{AB} [3 \times 5] & (\gamma_{s^*p}^{AB})^T \\ A'_s & & & & & & & (\gamma_{sd}^{AB})^* [1 \times 5] & (\gamma_{s^*s}^{AB})^* \\ A'_p & & & & & & & (-\gamma_{pd}^{AB})^* [3 \times 5] & (-\gamma_{s^*p}^{AB})^\dagger \\ B_s & & & & & & & \gamma_{sd}^{BB} [1 \times 5] & \gamma_{s^*s}^{BB} \\ B_p & & & & & & & \gamma_{pd}^{BB} [3 \times 5] & (\gamma_{s^*p}^{BB})^T \\ B_d & (\gamma_{sd}^{AB})^\dagger & (\gamma_{pd}^{AB})^\dagger & (\gamma_{sd}^{AB})^T & (-\gamma_{pd}^{AB})^T & (\gamma_{sd}^{BB})^\dagger & (\gamma_{pd}^{BB})^\dagger & \gamma_{dd}^{BB} & \gamma_{s^*d}^{BB} \\ & [5 \times 1] & [5 \times 3] & [5 \times 1] & [5 \times 3] & [5 \times 1] & [5 \times 3] & [5 \times 5] & [1 \times 5] \\ B_s^* & (\gamma_{s^*s}^{AB})^* & (\gamma_{s^*p}^{AB})^* & \gamma_{s^*s}^{AB} & -\gamma_{s^*p}^{AB} & (\gamma_{s^*s}^{BB})^* & (\gamma_{s^*p}^{BB})^\dagger & (\gamma_{s^*d}^{BB})^\dagger & (\gamma_{s^*s^*}^{BB}) \end{pmatrix}, \quad (\text{A3})$$

$$\gamma_{sp}(\mathbf{k}) = \begin{pmatrix} \mu & A_s & A_x & A_y & A_z & A'_s & A'_x & A'_y & A'_z & B_s & B_{px} & B_{py} & B_{pz} \\ A_s & \gamma_{ss}^{AA} & & & & \gamma_{ss}^{AA'} & & & & \gamma_{ss}^{AB} & & & \gamma_{sp}^{AB} \\ A_x & & & & & & & & & & & & \\ A_y & (\gamma_{sp}^{AA})^\dagger & & & & & & & & (\gamma_{sp}^{BA})^T & & & \gamma_{pp}^{AB} \\ A_z & & & & & & & & & & & & \\ A'_s & \gamma_{ss}^{AA'} & & & & & & & & (\gamma_{ss}^{AB})^* & & & -(\gamma_{sp}^{AB})^* \\ A'_x & & & & & & & & & & & & \\ A'_y & (\gamma_{sp}^{AA'})^\dagger & & & & & & & & (-\gamma_{sp}^{BA})^\dagger & & & (\gamma_{pp}^{AB})^* \\ A'_z & & & & & & & & & & & & \\ B_s & (\gamma_{ss}^{AB})^* & & & & & & & & \gamma_{ss}^{BB} & & & \gamma_{sp}^{BB} \\ B_{px} & & & & & & & & & & & & \\ B_{py} & (\gamma_{sp}^{AB})^\dagger & & & & & & & & (\gamma_{sp}^{BB})^\dagger & & & \gamma_{pp}^{BB} \\ B_{pz} & & & & & & & & & & & & \end{pmatrix}. \quad (\text{A4})$$

The interaction parameters defined in equations (A3) and (A4) are given by:

$$\gamma_{ss}^{AA'} = \gamma_{ss}^{A'A} = 2\sigma_{ss}^{AA} \left(\cos \frac{k_x}{2} + \cos \frac{k_y}{2} + \cos \frac{k_z}{2} \right), \quad (\text{A5})$$

$$\gamma_{ss}^{AA} = \gamma_{ss}^{A'A'} = 4\tilde{\sigma}_{ss}^{AA} \left(\cos \frac{k_x}{2} \cos \frac{k_y}{2} + \cos \frac{k_x}{2} \cos \frac{k_z}{2} + \cos \frac{k_y}{2} \cos \frac{k_z}{2} \right), \quad (\text{A6})$$

$$\gamma_{ss}^{BB} = 4\sigma_{ss}^{BB} \left(\cos \frac{k_x}{2} \cos \frac{k_y}{2} + \cos \frac{k_x}{2} \cos \frac{k_z}{2} + \cos \frac{k_y}{2} \cos \frac{k_z}{2} \right), \quad (\text{A7})$$

$$\gamma_{ss}^{AB} = (\gamma_{ss}^{A'B})^* = 4\sigma_{ss}^{AB} \left(\cos \frac{k_x}{4} \cos \frac{k_y}{4} \cos \frac{k_z}{4} - i \sin \frac{k_x}{4} \sin \frac{k_y}{4} \sin \frac{k_z}{4} \right), \quad (\text{A8})$$

$$\begin{aligned} \frac{\gamma_{pp}^{BB}}{2} = & t^{p_i p_j}(\delta_1^+) \cos \left(\frac{k_y}{2} + \frac{k_z}{2} \right) + t^{p_i p_j}(\delta_4^+) \cos \left(\frac{k_y}{2} - \frac{k_z}{2} \right) \\ & + t^{p_i p_j}(\delta_2^+) \cos \left(\frac{k_x}{2} + \frac{k_z}{2} \right) + t^{p_i p_j}(\delta_5^+) \cos \left(\frac{k_x}{2} - \frac{k_z}{2} \right) \\ & + t^{p_i p_j}(\delta_3^+) \cos \left(\frac{k_x}{2} + \frac{k_y}{2} \right) + t^{p_i p_j}(\delta_6^+) \cos \left(\frac{k_x}{2} - \frac{k_y}{2} \right), \end{aligned} \quad (\text{A9})$$

where

$$\begin{aligned} t^{p_i p_j}(\delta_1^+) &= \begin{pmatrix} \pi_{pp}^B & 0 & 0 \\ 0 & p_+ & p_- \\ 0 & p_- & p_+ \end{pmatrix} & t^{p_i p_j}(\delta_2^+) &= \begin{pmatrix} p_+ & 0 & p_- \\ 0 & \pi_{pp}^B & 0 \\ p_- & 0 & p_+ \end{pmatrix} & t^{p_i p_j}(\delta_3^+) &= \begin{pmatrix} p_+ & p_- & 0 \\ p_- & p_+ & 0 \\ 0 & 0 & \pi_{pp}^B \end{pmatrix} \\ t^{p_i p_j}(\delta_4^+) &= \begin{pmatrix} \pi_{pp}^B & 0 & 0 \\ 0 & p_+ & -p_- \\ 0 & -p_- & p_+ \end{pmatrix} & t^{p_i p_j}(\delta_5^+) &= \begin{pmatrix} p_+ & 0 & -p_- \\ 0 & \pi_{pp}^B & 0 \\ -p_- & 0 & p_+ \end{pmatrix} & t^{p_i p_j}(\delta_6^+) &= \begin{pmatrix} p_+ & -p_- & 0 \\ -p_- & p_+ & 0 \\ 0 & 0 & \pi_{pp}^B \end{pmatrix}. \end{aligned} \quad (\text{A10})$$

Here, $p_{\pm} \equiv (\sigma_{pp}^B \pm \pi_{pp}^B)/2$ where σ_{pp}^B and π_{pp}^B represent the σ and π bonds for the p orbitals of the B atoms. The elements $t^{p_i p_j}(\delta)[i,j]$ of (A10) represent the

coupling between orbitals p_i and p_j in the direction δ . The equivalent expressions for the A elements are obtained as:

$$\frac{\gamma_{pp}^{AA'}}{2} = \frac{\gamma_{pp}^{A'A}}{2} = \begin{pmatrix} \sigma_{pp}^A & 0 & 0 \\ 0 & \pi_{pp}^A & 0 \\ 0 & 0 & \pi_{pp}^A \end{pmatrix} \cos \frac{k_x}{2} + \begin{pmatrix} \pi_{pp}^A & 0 & 0 \\ 0 & \sigma_{pp}^A & 0 \\ 0 & 0 & \pi_{pp}^A \end{pmatrix} \cos k_y + \begin{pmatrix} \pi_{pp}^A & 0 & 0 \\ 0 & \pi_{pp}^A & 0 \\ 0 & 0 & \sigma_{pp}^A \end{pmatrix} \cos k_z. \quad (\text{A11})$$

$$\gamma_{pp}^{AA} = \gamma_{pp}^{A'A'} = \gamma_{pp}^{BB} [\sigma_{pp}^B \leftarrow \tilde{\sigma}_{pp}^A, \pi_{pp}^B \leftarrow \tilde{\pi}_{pp}^A], \quad (\text{A12})$$

where γ_{pp}^{BB} is given by (A9) with a new set of parameters, i.e. $\tilde{\sigma}_{pp}^A$ and $\tilde{\pi}_{pp}^A$. For the cross couplings AB, the interactions are given by:

$$\begin{aligned} \frac{\gamma_{pp}^{AB}}{4} = & \frac{(\gamma_{pp}^{A'B})^*}{4} = p_2^+ \begin{pmatrix} 1 & 0 & 0 \\ 0 & 1 & 0 \\ 0 & 0 & 1 \end{pmatrix} \left(\cos \frac{k_x}{4} \cos \frac{k_y}{4} \cos \frac{k_z}{4} - i \sin \frac{k_x}{4} \sin \frac{k_y}{4} \sin \frac{k_z}{4} \right) - p_2^- \begin{pmatrix} 0 & 1 & 0 \\ 1 & 0 & 0 \\ 0 & 0 & 0 \end{pmatrix} \\ & \times \left(\sin \frac{k_x}{4} \sin \frac{k_y}{4} \cos \frac{k_z}{4} - i \cos \frac{k_x}{4} \cos \frac{k_y}{4} \sin \frac{k_z}{4} \right) - p_2^- \begin{pmatrix} 0 & 0 & 1 \\ 0 & 0 & 0 \\ 1 & 0 & 0 \end{pmatrix} \left(\sin \frac{k_x}{4} \cos \frac{k_y}{4} \sin \frac{k_z}{4} - i \cos \frac{k_x}{4} \sin \frac{k_y}{4} \cos \frac{k_z}{4} \right) \\ & - p_2^- \begin{pmatrix} 0 & 0 & 0 \\ 0 & 0 & 1 \\ 0 & 1 & 0 \end{pmatrix} \left(\cos \frac{k_x}{4} \sin \frac{k_y}{4} \sin \frac{k_z}{4} - i \sin \frac{k_x}{4} \cos \frac{k_y}{4} \cos \frac{k_z}{4} \right), \end{aligned} \quad (\text{A13})$$

where $p_2^- \equiv (\sigma_{pp}^{AB} - \sigma_{pp}^{AB})/3$ and $p_2^+ \equiv (\sigma_{pp}^{AB} + 2\sigma_{pp}^{AB})/3$. Also,

$$\gamma_{sp}^{AA'} = \gamma_{sp}^{A'A} = 2i\sigma_{sp}^{AA} \left(\sin \frac{k_x}{2}, \sin \frac{k_y}{2}, \sin \frac{k_z}{2} \right), \quad (A15)$$

$$\gamma_{sp}^{BB} = 2\sqrt{2}i\sigma_{sp}^{BB} \left(\sin \frac{k_x}{2} \left(\cos \frac{k_y}{2} + \cos \frac{k_z}{2} \right), \right. \\ \left. \sin \frac{k_y}{2} \left(\cos \frac{k_z}{2} + \cos \frac{k_x}{2} \right), \sin \frac{k_z}{2} \left(\cos \frac{k_x}{2} + \cos \frac{k_y}{2} \right) \right), \quad (A14)$$

$$\gamma_{sp}^{AA} = \gamma_{sp}^{A'A'} = \gamma_{sp}^{BB} [\sigma_{sp}^B \leftarrow \tilde{\sigma}_{sp}^A], \quad (A16)$$

$$\gamma_{sp}^{AB} = -(\gamma_{sp}^{A'B})^* = -\frac{4\sigma_{sp}^{AB}}{\sqrt{3}} \left(\cos \frac{k_x}{4} \sin \frac{k_y}{4} \sin \frac{k_z}{4} - i \sin \frac{k_x}{4} \cos \frac{k_y}{4} \cos \frac{k_z}{4}, \right. \\ \left. \sin \frac{k_x}{4} \sin \frac{k_y}{4} \cos \frac{k_z}{4} - i \cos \frac{k_x}{4} \cos \frac{k_y}{4} \sin \frac{k_z}{4} \right), \quad (A17)$$

$$\gamma_{sp}^{BA} = -(\gamma_{sp}^{BA'})^* = \frac{\sigma_{sp}^{BA}}{\sigma_{sp}^{AB}} \gamma_{sp}^{AB}. \quad (A18)$$

The interaction of the d orbitals with those of s, p, d are summarized as follows:

$$\gamma_{dd} = \sum_{\delta \in \delta_{BB}^+} 2t_{dd}(\delta) \cos(\mathbf{k} \cdot \delta), \quad (A19)$$

$$t_{dd}(\delta) = \begin{pmatrix} 3l^2m^2 & 3lm^2n & 3l^2mn & \frac{3}{2}lm(l^2 - m^2) & \sqrt{3}lm[n^2 - \frac{1}{2}(l^2 + m^2)] \\ & 3m^2n^2 & 3lmn^2 & \frac{3}{2}mn(l^2 - m^2) & \sqrt{3}mn[n^2 - \frac{1}{2}(l^2 + m^2)] \\ & & 3l^2n^2 & \frac{3}{2}nl(l^2 - m^2) & \sqrt{3}nl[n^2 - \frac{1}{2}(l^2 + m^2)] \\ \text{T} & & \frac{3}{2}(l^2 - m^2)^2 & \sqrt{3}(l^2 - m^2)[n^2 - \frac{1}{2}(l^2 + m^2)] \\ & & & [n^2 - \frac{1}{2}(l^2 + m^2)]^2 \end{pmatrix} \sigma_{dd}$$

$$+ \begin{pmatrix} l^2 + m^2 - 4l^2m^2 & ln(1 - 4m^2) & mn(1 - 4l^2) & 2lm(m^2 - l^2) & -2\sqrt{3}lmn^2 \\ & m^2 + n^2 - 4m^2n^2 & lm(1 - 4n^2) & -mn[1 + 2(l^2 - m^2)] & \sqrt{3}mn(l^2 + m^2 - n^2) \\ & & l^2 + n^2 - 4l^2n^2 & nl[1 - 2(l^2 - m^2)] & \sqrt{3}ln(l^2 + m^2 - n^2) \\ \text{T} & & & l^2 + m^2 - (l^2 - m^2)^2 & \sqrt{3}n^2(m^2 - l^2) \\ & & & & 3n^2(l^2 + m^2) \end{pmatrix} \pi_{dd}$$

$$+ \begin{pmatrix} n^2 + l^2m^2 & ln(m^2 - 1) & mn(l^2 - 1) & \frac{1}{2}lm(l^2 - m^2) & \frac{\sqrt{3}}{2}lm(1 + n^2) \\ & l^2 + m^2n^2 & lm(n^2 - 1) & mn(1 + \frac{1}{2}(l^2 - m^2)) & -\frac{\sqrt{3}}{2}mn(l^2 + m^2) \\ & & m^2 + l^2n^2 & -nl(1 - \frac{1}{2}(l^2 - m^2)) & -\frac{\sqrt{3}}{2}ln(l^2 + m^2) \\ \text{T} & & & n^2 + \frac{1}{4}(l^2 - m^2)^2 & \frac{\sqrt{3}}{4}(1 + n^2)(l^2 - m^2) \\ & & & & \frac{3}{4}(l^2 + m^2)^2 \end{pmatrix} \delta_{dd}, \quad (A20)$$

in which σ_{dd} , π_{dd} and δ_{dd} are the hopping parameters, and T denotes the transpose of the upper-triangular matrix. δ_{BB}^+ is the half of the BB vectors presented in table 1 with a positive sign. Also, $\{l, m, n\}$ are respectively the x, y and z components of the direction of δ .

$$\gamma_{pd}^{BB} = \sum_{\delta \in \delta_{BB}^+} 2it_{pd}(\delta) \sin(\mathbf{k} \cdot \delta), \quad (A21)$$

where $t_{pd}(\delta)$ is the p - d interaction matrix given by:

$$t_{pd}(\delta) = \begin{pmatrix} \sqrt{3}l^2m & \sqrt{3}lmn & \sqrt{3}l^2n & \frac{\sqrt{3}}{2}l(l^2 - m^2) & l[n^2 - \frac{1}{2}(l^2 + m^2)] \\ \sqrt{3}lm^2 & \sqrt{3}m^2n & \sqrt{3}lmn & \frac{\sqrt{3}}{2}m(l^2 - m^2) & m[n^2 - \frac{1}{2}(l^2 + m^2)] \\ \sqrt{3}lmn & \sqrt{3}mn^2 & \sqrt{3}ln^2 & \frac{\sqrt{3}}{2}n(l^2 - m^2) & n[n^2 - \frac{1}{2}(l^2 + m^2)] \end{pmatrix} \sigma_{pd} + \begin{pmatrix} m(1 - 2l^2) & -2lmn & n(1 - 2l^2) & l(1 - l^2 + m^2) & -\sqrt{3}ln^2 \\ l(1 - 2m^2) & m(1 - 2m^2) & -2lmn & -m(1 + l^2 - m^2) & -\sqrt{3}mn^2 \\ -2lmn & m(1 - 2n^2) & l(1 - 2n^2) & -n(l^2 + m^2) & \sqrt{3}n(l^2 + m^2) \end{pmatrix} \pi_{pd}. \quad (A22)$$

For the γ_{pd}^{AB} interaction, no significant simplifications are available, and it is most convenient to use equation (2) directly,

$$\gamma_{pd}^{AB} = \sum_{\delta \in \delta_{AB}} t_{pd}(\delta) \exp(i\mathbf{k} \cdot \delta). \quad (A23)$$

Finally, the interaction between the s and d orbitals can be expressed by:

$$\gamma_{sd}^{BB} = \sum_{\delta \in \delta_{BB}^+} 2t_{sd}(\delta) \cos(\mathbf{k} \cdot \delta), \quad (A24)$$

$$t_{sd}^{BB}(\delta) = \sigma_{sd}^{BB} \left(\sqrt{3}lm, \sqrt{3}mn, \sqrt{3}ln, \frac{\sqrt{3}}{2}(l^2 - m^2), n^2 - \frac{1}{2}(l^2 + m^2) \right), \quad (A25)$$

and γ_{sd}^{AB} is found to be:

$$\gamma_{sd}^{AB} = (\gamma_{sd}^{A'B})^* = \frac{\sigma_{sd}^{AB}}{\sigma_{sp}^{AB}} \left(\gamma_{sp_z}^{AB}, \gamma_{sp_x}^{AB}, \gamma_{sp_y}^{AB}, 0, 0 \right). \quad (A26)$$

A virtual s^* orbital may be introduced into the formulations to represent the $4s/5s/6s/7s$ orbitals of Si/Ge/Sn/Pb in order to obtain better fittings with less deviations with respect to the DFT band structure. The interaction integrals, corresponding to s^* , can be calculated using:

$$\gamma_{s^*\mu}^{B\alpha} = \frac{\sigma_{s^*\mu}^{B\alpha}}{\sigma_{s\mu}^{B\alpha}} \gamma_{s\mu}^{B\alpha}, \quad \gamma_{s^*s^*}^{BB} = \frac{\sigma_{s^*s^*}^{BB}}{\sigma_{ss}^{BB}} \gamma_{ss}^{BB}, \quad \alpha = \{A, A', B\}, \quad \mu = \{s, p, d\}. \quad (A27)$$

Also, we may summarize the p orbital matrix elements for the SOI operator $\eta_{\mu\nu, \sigma\sigma'}$ as:

$$\eta_{p_i p_j \sigma \sigma'} = \frac{\eta_{SO}}{2} \begin{pmatrix} p_{i\sigma} & p_{x\uparrow} & p_{x\downarrow} & p_{y\uparrow} & p_{y\downarrow} & p_{z\uparrow} & p_{z\downarrow} \\ p_{x\uparrow} & 0 & 0 & -i & 0 & 0 & 1 \\ p_{x\downarrow} & 0 & 0 & 0 & i & -1 & 0 \\ p_{y\uparrow} & i & 0 & 0 & 0 & 0 & -i \\ p_{y\downarrow} & 0 & -i & 0 & 0 & -i & 0 \\ p_{z\uparrow} & 0 & -1 & 0 & i & 0 & 0 \\ p_{z\downarrow} & 1 & 0 & i & 0 & 0 & 0 \end{pmatrix}. \quad (A28)$$

Appendix B. The total band structure using the machine-learned eighteen-band TB model

As pointed out in the main text, the deviation of the conduction bands in our machine-learned five-band TB model originates from the truncation of the more complete basis set given by equation (A1). A full conduction band is a complicated hybridization of different excited orbitals such as the d orbitals in Mg_2X . To show how the inclusion of higher excited states in our TB models can improve the fitting of conduction bands in the five-band TB model, we have employed the largest TB model we constructed, i.e. the eighteen-band TB model, and plotted its results in figure 7. We have considered a representative case where strain is set to zero and $\text{X} = \text{Ge}$. The dashed red curves are the DFT band structure whereas the solid blue curves are the band structure from our machine-learned eighteen-band TB model. Compared to figure 3(b2), we clearly see that the conduction bands are now greatly improved and more delicate features are captured by the eighteen-band TB model. The same improvement is accessible through the eighteen-band TB model when applied to the cases shown in figure 3.

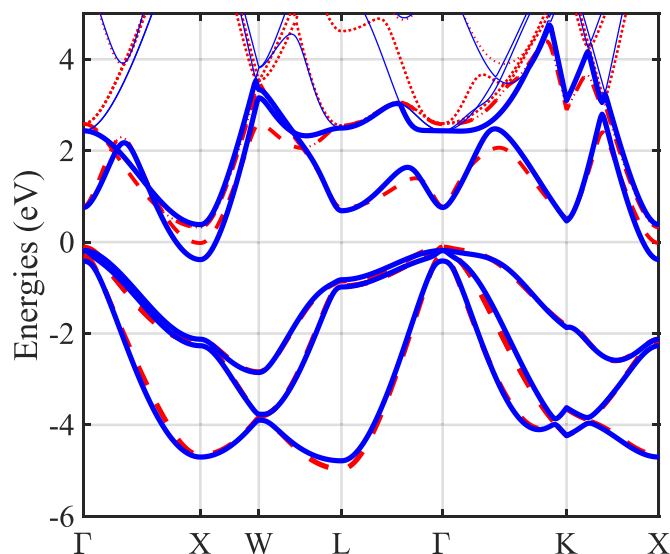


Figure 7. The band structure of Mg_2Ge along the high-symmetry path $\Gamma\text{XWL}\Gamma\text{KX}$. The strain is set to zero and the Fermi level is shifted to $E = 0$. The solid curves belong to the machine-learned eighteen-band TB model whereas the dashed curves are obtained by DFT.

Table 4. Hopping parameters, on-site energies, and spin–orbit coupling strength for the five-band TB model.

Strain	Type	AA		BB		AB	On-site		SOC
		σ_{ss} (eV)	$\tilde{\sigma}_{ss}$ (eV)	σ_{pp} (eV)	π_{pp} (eV)	σ_{sp} (eV)	E_{As} (eV)	E_{Bp} (eV)	η_{SO} (eV)
$\varepsilon = -10\%$	Si	0.0400	0.1036	0.6370	0.0002	0.6559	1.9654	−2.6307	0.0190
	Ge	0.0793	0.1092	0.6251	0.0039	0.7674	2.0422	−2.6611	0.1234
	Sn	0.0327	0.0955	0.6451	0.0147	0.6695	1.5619	−2.8796	0.3059
	Pb	−0.0955	0.0932	0.5718	0.0344	0.9046	0.9047	−3.0787	1.0731
$\varepsilon = 0$	Si	−0.0759	0.0660	0.4952	0.0052	0.6642	1.3375	−2.2480	0.0190
	Ge	−0.1499	0.0587	0.4362	0.0233	0.8279	1.0853	−2.1530	0.1220
	Sn	−0.0762	0.0678	0.4430	0.0281	0.7744	0.8680	−2.1290	0.2836
	Pb	−0.1913	0.0479	0.3936	0.0451	0.8707	0.4543	−2.0863	0.9174
$\varepsilon = +10\%$	Si	−0.1600	0.0454	0.3044	0.0304	0.7843	0.6505	−1.5692	0.0186
	Ge	−0.2273	0.0331	0.2730	0.0425	0.8346	0.4864	−1.4543	0.1135
	Sn	−0.1388	0.0590	0.1994	0.0632	0.8655	0.1442	−1.2072	0.2777
	Pb	−0.2220	0.0400	0.1733	0.0738	0.8700	−0.1516	−1.1477	0.8055

Appendix C. Machine-learning obtained parameters to the five-band TB model

Table 4 summarizes the optimized bonding parameter values obtained for the five-band TB model, presented in the main text, to describe Mg_2X ($\text{X} = \text{Si}, \text{Ge}, \text{Sn}, \text{Pb}$). We have included the obtained parameter values when strain is $\varepsilon = 0\%, \pm 10\%$. The presented bonding parameter values, on-site energies, and spin–orbit coupling strength η_{SO} in table 4 reproduce the valence band structure within the entire Brillouin zone.

ORCID iD

Mohammad Alidoust  <https://orcid.org/0000-0002-1554-687X>

References

- [1] Grosch G H and Range K-J 1996 Studies on AB_2 -type intermetallic compounds. I. Mg_2Ge and Mg_2Sn : single-crystal structure refinement and *ab initio* calculations *J. Alloys Compd.* **235** 250
- [2] Nozariab A *et al* 2017 Thermoelectric silicides: a review *J. Appl. Phys.* **56** 05DA04
- [3] Muthiah S, Pulikkotil J, Srivastava A, Kumar A, Pathak B, Dhar A and Budhani R 2013 Conducting grain boundaries enhancing thermoelectric performance in doped Mg_2Si *Appl. Phys. Lett.* **103** 053901
- [4] Kamila H, Sahu P, Sankhla A, Yasseri M, Pham H-N, Dasgupta T, Muellerab E and de Boer J 2019 Analyzing transport properties of p-type Mg_2Si – Mg_2Sn solid solutions: optimization of thermoelectric performance and insight into the electronic band structure *J. Mater. Chem. A* **7** 1045
- [5] Zhou Z, Chai Y W, Ikuta Y, Lee Y, Lin Y and Kimura Y 2020 Reduced thermal conductivity of $\text{Mg}_2(\text{Si}, \text{Sn})$ solid solutions by a gradient composition layered microstructure *ACS Appl. Mater. Interfaces* **12** 17
- [6] Sankhla A, Kamila H, Naithani H, Mueller E and de Boer J 2021 On the role of Mg content in $\text{Mg}_2(\text{Si}, \text{Sn})$: assessing its impact on electronic transport and estimating the phase width by *in situ* characterization and modelling *Mater. Today Phys.* **21** 100471

- [7] Ryu B, Choi E-A, Park S, Chung J, de Boor J, Ziolkowski P, Muller E and Park S 2021 Native point defects and low p-doping efficiency in $\text{Mg}_2(\text{Si}, \text{Sn})$ solid solutions: a hybrid-density functional study *J. Alloys Compd.* **853** 157145
- [8] Shi G and Kioupakis E 2018 Relativistic quasiparticle band structures of Mg_2Si , Mg_2Ge and Mg_2Sn : consistent parameterization and prediction of Seebeck coefficients *J. Appl. Phys.* **123** 085114
- [9] Kim S, Wiendlocha B, Jin H, Tobola J and Heremans J P 2014 Electronic structure and thermoelectric properties of p-type Ag-doped Mg_2Sn and $\text{Mg}_2\text{Sn}_{1-x}\text{Si}_x$ *J. Appl. Phys.* **116** 153706
- [10] Zwolenski P, Tobola J and Kaprzyk S 2011 A theoretical search for efficient dopants in Mg_2X ($\text{X} = \text{Si}, \text{Ge}, \text{Sn}$) thermoelectric materials *J. Electron. Mater.* **40** 889
- [11] Zwolenski P, Tobola J and Kaprzyk S 2015 KKR-CPA study of electronic structure and relative stability of Mg_2X ($\text{X} = \text{Si}, \text{Ge}, \text{Sn}$) thermoelectrics containing point defects *J. Alloys Compd.* **627** 85
- [12] Kamila H, Sankhla A, Yasserli M, Mueller E and de Boor J 2020 Non-rigid band structure in Mg_2Ge for improved thermoelectric performance *Adv. Sci.* **7** 2000070
- [13] de Boor J, Berche A and Jund P 2020 Density of states effective mass for p-type Mg_2Si – Mg_2Sn solid solutions: comparison between experiments and first-principles calculations *J. Phys. Chem. C* **124** 14987
- [14] Guerra J M, Mahr C, Giar M, Czerner M and Heiliger C 2018 *Ab initio* calculations of electronic band structure and effective-mass parameters of thermoelectric $\text{Mg}_2\text{X}_{1-x}\text{Y}_x$ ($\text{X}, \text{Y} = \text{Si}, \text{Ge}, \text{Sn}$) pseudobinary alloys *Phys. Rev. Mater.* **2** 104605
- [15] Pulikkotil J J, Singh D J, Auluck S, Saravanan M, Misra D K, Dhar A and Budhani R C 2012 Doping and temperature dependence of thermoelectric properties in $\text{Mg}_2(\text{Si}, \text{Sn})$ *Phys. Rev. B* **86** 155204
- [16] Tan X J, Liu W, Liu H J, Shi J, Tang X F and Uher C 2012 Multiscale calculations of thermoelectric properties of n-type $\text{Mg}_2\text{Si}_{1-x}\text{Sn}_x$ solid solutions *Phys. Rev. B* **85** 205212
- [17] Jiang G, Chen L, He J, Gao H, Du Z, Zhao X, Tritt T M and Zhu T 2013 Improving p-type thermoelectric performance of $\text{Mg}_2(\text{Ge}, \text{Sn})$ compounds via solid solution and Ag doping *Intermetallics* **32** 312
- [18] Liu W *et al* 2015 n-Type thermoelectric material $\text{Mg}_2\text{Sn}_{0.75}\text{Ge}_{0.25}$ for high power generation *Proc. Natl Acad. Sci.* **112** 3269
- [19] Mao J, Kim H S, Shuai J, Liu Z, He R, Saparamadu U, Tian F, Liu W and Ren Z 2016 Thermoelectric properties of materials near the band crossing line in Mg_2Sn – Mg_2Ge – Mg_2Si system *Acta Mater.* **103** 633
- [20] Yasserli M, Mitra K, Sankhla A, de Boor J and Muller E 2021 Influence of Mg loss on the phase stability in Mg_2X ($\text{X} = \text{Si}, \text{Sn}$) and its correlation with coherency strain *Acta Mat.* **208** 116737
- [21] Yelgel O C and Yelgel C 2019 Thermoelectric transport behaviours of n-type $\text{Mg}_2(\text{Si}, \text{Sn}, \text{Ge})$ quaternary solid solutions *J. Magnesium Alloys* **7** 514
- [22] Hu X, Jood P, Ohta M, Kunii M, Nagase K, Nishiate H, Kanatzidis M G and Yamamoto A 2016 Power generation from nanostructured PbTe-based thermoelectrics: comprehensive development from materials to modules *Energy Environ. Sci.* **9** 517
- [23] Tang X, Zhang Y, Zheng Y, Peng K, Huang T, Lu X, Wang G, Wang S and Zhou X 2017 Improving thermoelectric performance of p-type Ag-doped $\text{Mg}_2\text{Si}_{0.4}\text{Sn}_{0.6}$ prepared by unique melt spinning method *Appl. Therm. Eng.* **111** 1396
- [24] Kraemer D *et al* 2011 High-performance flat-panel solar thermoelectric generators with high thermal concentration *Nat. Mater.* **10** 532
- [25] Kutorasinski K, Wiendlocha B, Tobola J and Kaprzyk S 2014 Importance of relativistic effects in electronic structure and thermopower calculations for Mg_2Si , Mg_2Ge and Mg_2Sn *Phys. Rev. B* **89** 115205
- [26] Sobolev V V, Kalugin A I and Antonov E A 2021 Parameters of fundamental optical functions and elementary transition bands for Mg_2X compounds ($\text{X} = \text{Si}, \text{Ge}, \text{Sn}$) *J. Appl. Spectrosc.* **88** 137
- [27] Shi X, Yang J, Salvador J R, Chi M, Cho J Y, Wang H, Bai S, Yang J, Zhang W and Chen L 2011 Multiple-filled skutterudites: high thermoelectric figure of merit through separately optimizing electrical and thermal transports *J. Am. Chem. Soc.* **133** 7837
- [28] Espinosa N, Lazard M, Aixala L and Scherrer H 2010 Modeling a thermoelectric generator applied to diesel automotive heat recovery *J. Electron. Mater.* **39** 1446
- [29] Zhu H, Sun W, Armiento R, Lazic P and Ceder G 2014 Band structure engineering through orbital interaction for enhanced thermoelectric power factor *Appl. Phys. Lett.* **104** 082107
- [30] Bai G, Tian J, Guo Q, Li Z and Zhao Y 2021 First principle study on Mg_2X ($\text{X} = \text{Si}, \text{Ge}, \text{Sn}$) intermetallics by Bi micro-alloying *Crystals* **11** 142
- [31] Bao L, Kong Z, Qu D and Duan Y 2020 Revealing the elastic properties and anisotropies of Mg_2X ($\text{X} = \text{Si}, \text{Ge}, \text{Sn}$) T with different structures from a first-principles calculation *Mater. Today Commun.* **24** 101337
- [32] Bao L, Kong Z, Qu D and Duan Y 2020 Insight of structural stability, elastic anisotropies and thermal conductivities of Y, Sc doped Mg_2Pb from first-principles calculations *Chem. Phys. Lett.* **756** 137833
- [33] Murtaza G, Sajid A, Rizwan M, Takagiwa Y, Khachai H, Jibrani M, Khenata R and Bin Omran S 2015 First principles study of Mg_2X ($\text{X} = \text{Si}, \text{Ge}, \text{Sn}, \text{Pb}$): elastic, optoelectronic and thermoelectric properties *Mater. Sci. Semicond. Process.* **40** 429
- [34] Balout H, Boulet P and Record M-C 2014 Electronic and transport properties of Mg_2Si under isotropic strains *Intermetallics* **50** 8
- [35] Arnaud B and Alouani M 2001 Electron-hole excitations in Mg_2Si and Mg_2Ge compounds *Phys. Rev. B* **64** 033202
- [36] Mizoguchi H, Muraba Y, Fredrickson D C, Matsuishi S, Kamiya T and Hosono H 2017 The unique electronic structure of Mg_2Si : shaping the conduction bands of semiconductors with multicenter bonding *Angew. Chem., Int. Ed.* **56** 10135
- [37] Fan T, Xie C, Wanga S, Oganov A R and Cheng L 2018 First-principles study of thermoelectric properties of Mg_2Si – Mg_2Pb semiconductor materials *RSC Adv.* **8** 17168
- [38] El Ahmar Y, Hallouche A, Dahani A, Zaoui A, Kacimi S, Haddouche Z, Djebari M and Boukourt A 2019 First-principle simulation of ferromagnetism in Gd-doped Mg_2X ($\text{X} = \text{Si}, \text{Ge}$ and Sn) *SPIN* **09** 1950010
- [39] Alidoust M, Kleiven D and Akola J 2020 Density functional simulations of pressurized Mg–Zn and Al–Zn alloys *Phys. Rev. Mater.* **4** 045002
- [40] Slater J C and Koster G F 1954 Simplified LCAO method for the periodic potential problem *Phys. Rev.* **94** 1498
- [41] Winkler R 2003 *Spin-Orbit Coupling Effects in Two-Dimensional Electron and Hole Systems* 3rd edn (Berlin: Springer)
- [42] Russell S and Norvig P 2001 *Artificial Intelligence: A Modern Approach (Prentice Hall Series in Artificial Intelligence)* (Hoboken, NJ: Prentice Hall)
- [43] Ingber L and Rosen B 1992 Genetic algorithms and very fast simulated reannealing: a comparison *Math. Comp. Model.* **16** 87

- [44] Enkovaara J *et al* 2010 Electronic structure calculations with GPAW: a real-space implementation of the projector augmented-wave method *J. Phys.: Condens. Matter* **22** 253202
- [45] Alidoust M, Willatzen M and Jauho A-P 2019 Control of superconducting pairing symmetries in monolayer black phosphorus *Phys. Rev. B* **99** 125417
- [46] Winkler U 1955 Electrical properties of the intermetallic compounds Mg_2Si , Mg_2Ge , Mg_2Sn , Mg_2Pb *Helv. Phys. Acta* **28** 633
- [47] Lott L A and Lynch D W 1966 Infrared absorption in Mg_2Ge *Phys. Rev.* **141** 681
- [48] Vazquez F, Forman A R and Cardonna M 1968 Electroreflectance measurements on Mg_2Si , Mg_2Ge , Mg_2Sn *Phys. Rev.* **176** 905
- [49] Lee P M 1964 Electronic structure of magnesium silicide and magnesium germanide *Phys. Rev.* **135** 1110
- [50] Au-Yang M Y and Cohen M L 1969 Electronic structure and optical properties of Mg_2Si , Mg_2Ge , Mg_2Sn *Phys. Rev.* **178** 1358